PROCEEDINGS OF SCIENCE

Refinement of the High-Energy Gamma-ray Selection for CALET on the International Space Station

Nicholas Cannady[a,b,c,*] **for the CALET collaboration**

[a] *Center for Space Sciences and Technology, University of Maryland, Baltimore County, 1000 Hilltop Circle, Baltimore, Maryland 21250, USA*

[b] *Astroparticle Physics Laboratory, NASA/GSFC, Greenbelt, Maryland 20771, USA*

[c] *Center for Research and Exploration in Space Sciences and Technology, NASA/GSFC, Greenbelt, Maryland 20771, USA*

E-mail: nicholas.w.cannady@nasa.gov

The Calorimetric Electron Telescope (CALET) is a deep electromagnetic calorimeter designed for the measurement of cosmic-ray electrons on the International Space Station. Deployed on the Exposed Facility of the Japanese Experiment Module since August 2015, it observes cosmic-ray electrons with energies up to above 10 TeV and hadrons up to PeV total energies. It is also sensitive to gamma rays in the energy range from 1 GeV to 1 TeV. At energies above 100 GeV, sensitivity is lost in the gamma-ray selection as previously defined. This is due in large part to the contamination of the charge measurement in the CHD (Charge Detector) and the IMC (Imaging Calorimeter) by backscattered particles from the electromagnetic shower in the TASC (Total Absorption Calorimeter). In this work, we implement a revision to the photon selection criteria using a significantly increased simulated dataset, increasing CALET's exposure at these energies significantly. Furthermore, the allowable geometry for incident photons is expanded and the energy reconstruction revised to tighten the energy resolution for highly inclined tracks. We validate the distributions used for the selection through comparison with real data, evaluate the changes to the instrument response functions, and assess the implications for the flight data analysis of gamma rays with CALET.

38th International Cosmic Ray Conference (ICRC2023)
26 July - 3 August, 2023
Nagoya, Japan

ICRC2023
38th International Cosmic Ray Conference
The Astroparticle Physics Conference

*Speaker

PoS(ICRC2023)657

1. Introduction

The Calorimetric Electron Telescope (CALET) is an International Space Station (ISS)-borne astroparticle physics instrument designed to measure the spectrum of cosmic-ray electrons in the GeV–TeV energy range to search for signatures of nearby sources or dark matter [1]. In addition to cosmic-ray electrons, the CALET calorimeter is sensitive to gamma rays in the 1-1000 GeV range and cosmic-ray hadrons up to PeV total energies. Deployed on the Japanese Experiment Module Exposed Facility (JEM-EF) since August 2015, CALET has maintained stable data collection for over seven years.

The CALET gamma-ray selection has been previously optimized for the identification of photons at low energies [2] to prioritize counterpart searches for gravitational wave events [3–5]. Scientific analyses have also been performed to investigate quiescent Solar gamma rays, Galactic diffuse and point sources [6], and dark matter line signals [7]. These efforts would all benefit from improved performance in the high-energy region (above ~10 GeV). To that end, this work is a status report for an ongoing effort to expand the allowed geometries for high-energy (HE) trigger [8] events and to revise the event selection conditions to better preserve photon events at these energies.

2. Instrument

The CALET calorimeter comprises three main subsystems: the Charge Detector (CHD), the Imaging Calorimeter (IMC), and the Total Absorption Calorimeter (TASC). The CHD contains two layers of 14 plastic scintillating paddles each, arranged for segmentation along the X and Y directions, respectively. The IMC is eight pairs of crossed XY layers of 448 fine scintillating plastic fibers read out with multi-anode photomultipliers (MaPMTs). In order to stimulate first interaction and shower development in the IMC, tungsten sheets are placed between sets of layers such that normal incidence particles have passed three radiation lengths when reaching the last layer. Below the IMC, the TASC contains 12 crossed layers of lead tungstate logs for a total subsystem thickness of 27 radiation lengths. The TASC is able to fully contain electromagnetic showers up to TeV energies, maintaining a fine energy resolution over the operational range of the HE trigger [9].

3. Gamma-ray event reconstruction

Events for the gamma-ray analysis are selected from the low-energy gamma (LEG) and HE triggers. Tracks are fitted with both the electromagnetic shower tracking [10] and the CC track [2] algorithms, and events that are poorly fitted or which use fewer than three layers in both projections of the IMC are excluded. For this work, we show results for the EM track only, as the backgrounds with the CC Track at higher energies are still being investigated. Events are further filtered by the application of an offline trigger (appropriate to the LEG or HE trigger thresholds, depending on operational mode) to avoid efficiency fluctuations from small changes in the hardware trigger with changes in temperature, etc. After these simple requirements, the selection becomes dependent on the geometrical condition satisfied by the reconstructed track.

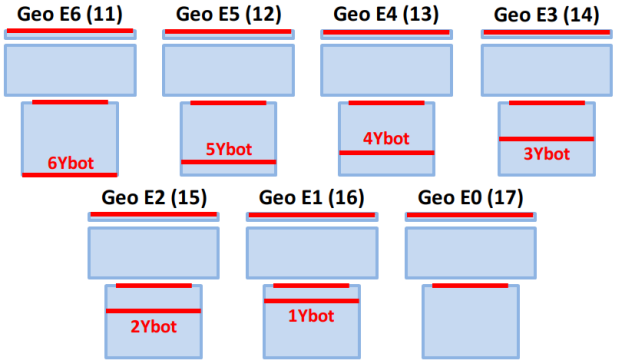

Geo.	Requirements	GF (cm2sr)	Inc. GF (cm2sr)
E6 (11)	CHDtop & TASCtop* & TASC6Ybot	510.13	510.14
E5 (12)	CHDtop & TASCtop* & TASC5Ybot	82.05	592.18
E4 (13)	CHDtop & TASCtop* & TASC4Ybot	99.22	691.40
E3 (14)	CHDtop & TASCtop* & TASC3Ybot	120.18	811.60
E2 (15)	CHDtop & TASCtop* & TASC2Ybot	144.18	955.77
E1 (16)	CHDtop & TASCtop* & TASC1Ybot	161.18	1116.95
E0 (17)	CHDtop & TASCtop*	67.47	1184.42

Figure 1: Preliminary new acceptance definitions for CALET calorimeter photon analyses. Geometries are defined exclusively, such that stepping from E6->E0 require shorter pathlengths through the TASC. These differ from the standard CALET acceptance conditions in that shorter TASC pathlengths are allowed, but passage through the CHD is always required for the charge measurement. The total geometrical factor for all seven conditions is comparable to that for standard acceptances A–D.

3.1 Revised geometrical acceptance

In revisiting the gamma-ray selection conditions, we have implemented a change in the definitions of the geometrical conditions applied for the photon analysis. These are shown graphically in Figure 1, along with the geometrical factors of each based purely on the detector geometry. These newly defined geometries are more clearly understood by their labels (E6 requires passage through all 6 pairs of PWO layers in the TASC, E5 requires passage through 5 pairs, and so on) and allow for tailored inclusion based on the required energy resolution for any given analysis. For the purposes of this work and the derivation of the instrument response, we consider these geometries exclusively. That is, events which satisfy E6 will not be included in the sample for E5, and so on. The shorter pathlengths through the TASC at the less restrictive geometries sacrifice the containment of showers at higher energies, and the impact on energy resolution is detailed in the section below.

3.2 Updated energy reconstruction

In reconstructing the primary energy of gamma-ray events, we consider energy deposits in the IMC and TASC. Generally, an energy estimator is calculated based on the deposits in the IMC and TASC layers, and a function is derived based on simulations to map that estimator to a mean primary energy. In calculating the energy estimator, we correct the energy deposit sum in the IMC with a Monte-Carlo derived and experimentally validated factor accounting for absorption in the passive tungsten sheets. For the TASC layers, we use only the 5 closest PWO logs to the reconstructed track intersection with each layer. In order to suppress noise contributions to the estimator, we have derived inclusion thresholds for successively deeper layers based on the energy deposited in each layer and in the TASC as a whole. Although the focus of this work is the improvement for events at higher energies, we have found that the energy resolution below 5 GeV is improved significantly by implementing this noise suppression in the estimator. Note that the correction functions for each geometrical acceptance condition are determined and applied separately to maintain the best performance for each class of events.

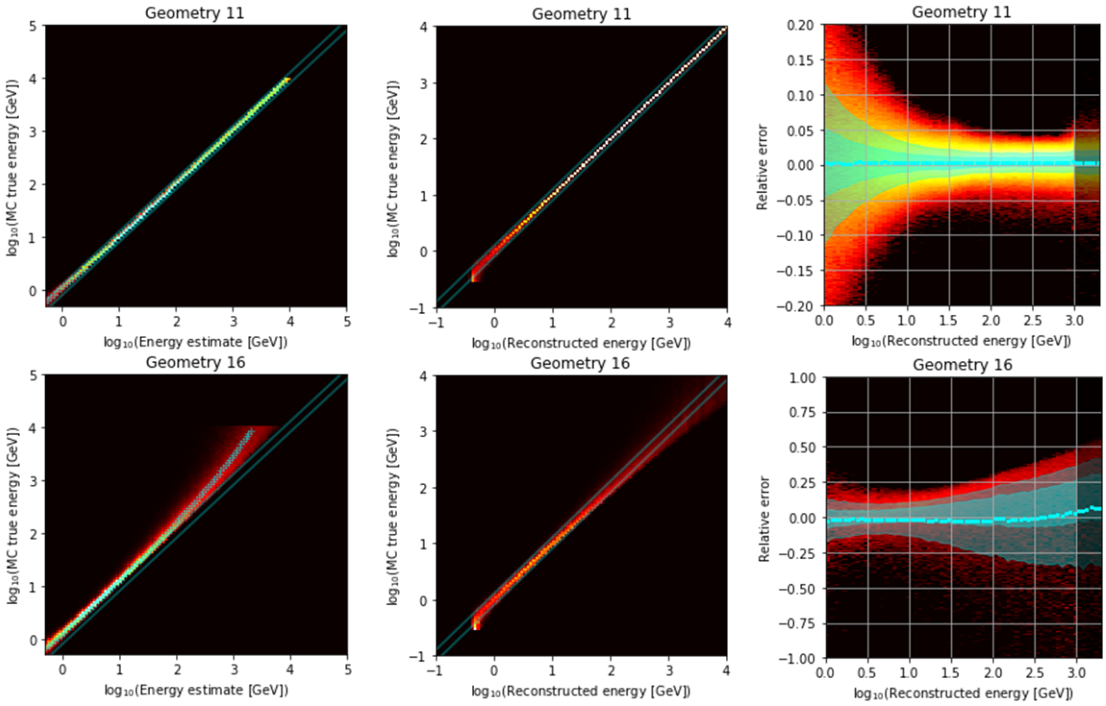

Figure 2: Illustration of energy reconstruction for geometries E6 (top row) and E1 (bottom row). The first column shows the MC true incident photon energy vs. the energy estimator from IMC and TASC deposits. Cyan diagonals are present to guide the eye, and cyan crosses show the mean energy estimator corresponding to each bin in MC true energy. The middle column shows the true energy plotted against the reconstructed energy after the correction function is applied. The rightmost column shows the error in the reconstructed energy plotted against the reconstructed energy. Cyan points illustrate the mean error in each bin of reconstructed energy, and the shaded regions indicate 33% and 67% containment.

In Figure 2 the performance of the energy reconstruction is illustrated. Geometries E6 (best containment) and E1 (low containment) are chosen to show the trend as the required pathlength in the TASC decreases. In the first column, the cyan points are the data points used to create the correction function which maps the energy estimator to reconstructed energy (the correction function interpolates between these). In the middle column, the correction function has been applied to calculate the reconstructed energy, which is now used as the abscissa. The third column now shows the relative error in the reconstructed energy (note the difference in y-scale for geometry E1 as compared to E6). The mean of the error in each bin of reconstructed energy lies close to zero up to TeV energies, although the distribution is increasingly asymmetric as energy increases and containment of the shower in the TASC worsens. We find that this asymmetry is minimal in geometries E6, E5, and E4 (with σ ~3-4% between 10-1000 GeV). For geometry E3 the asymmetry for the 33% containment region becomes clear above 100 GeV, although the 1-σ error remains symmetric and on the order of 5% up to 1 TeV. For geometries E2, E1, and E0, the error is further skewed at the 33% level, with the 1-σ errors reaching 15%, 30%, and 50% at several hundred GeV, respectively. We conclude that these geometries can still be used if either the sensitivity to any signal is more significant than the energy resolution requirements for an analysis or if the energy

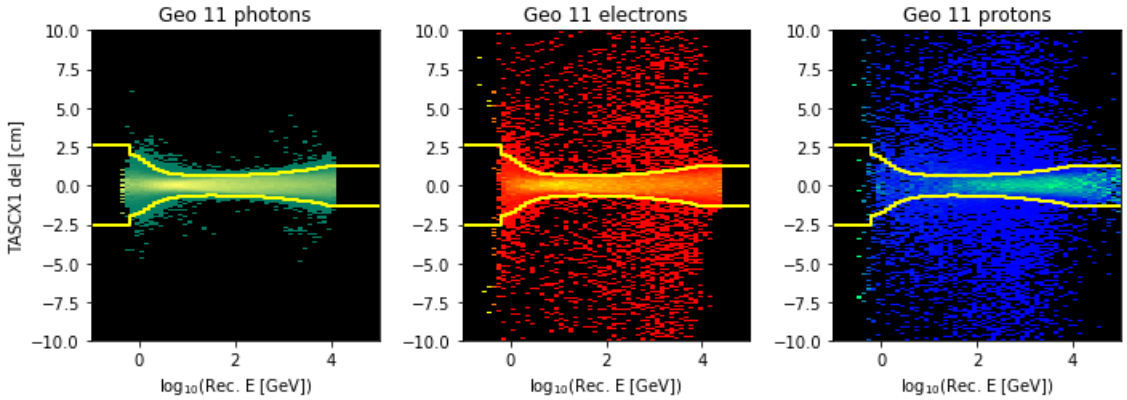

Figure 3: Heat maps of the difference between the center-of-energy in TASC X1 and the reconstructed track intersection point with the midplane of the same layer for geometry E6 as a function of reconstructed energy. The three columns show simulated photons, electrons, and protons, respectively. The yellow curve shows the 99% containment contour for in-geometry photon events.

range of interest is below 100 GeV.

3.3 Selection conditions

Further event selection conditions are now applied as a function of the reconstructed energy and the acceptance condition satisfied by the reconstructed track. A number of quality cuts are applied to reject poorly reconstructed events. These quantities are meant to isolate well-reconstructed electromagnetic showers and to reject hadronic events. To determine the thresholds for each of these cuts as a function of energy, simulated photons with MC true trajectory and reconstructed trajectory both satisfying the acceptance condition are analyzed and a variable threshold depending on how well-contained the distribution of the selection parameter is determined such that 90-98% of the well-reconstructed photons are preserved. These cuts are then analyzed for how well they reject hadrons and misreconstructed events.

Figure 3 shows an example of such a quality cut. The parameter being evaluated (TASC X1 delta) is the distance between the center of energy in TASC X1 layer and the reconstructed track intersection point with the TASC X1 midplane. For events with well-reconstructed showers, this will be near 0. The left, center, and right panels show MC photons, electrons, and protons, respectively, which were reconstructed in geometry E6. Electrons and protons whose MC true tracks are out-of-geometry are included if their reconstructed tracks are in-geometry, leading to the "fuzz" around the horizontal distribution. The yellow lines show the 98% containment threshold for the in-geometry simulated photons, and events outside of this contour are rejected.

The quality cuts applied in the revised photon selection are:

- TASC X1 delta: as above
- TASC Y1 delta: as with TASC X1 delta
- IMC Shower development: sum of IMC X8 and IMC Y8 deposits in fibers nearest track)

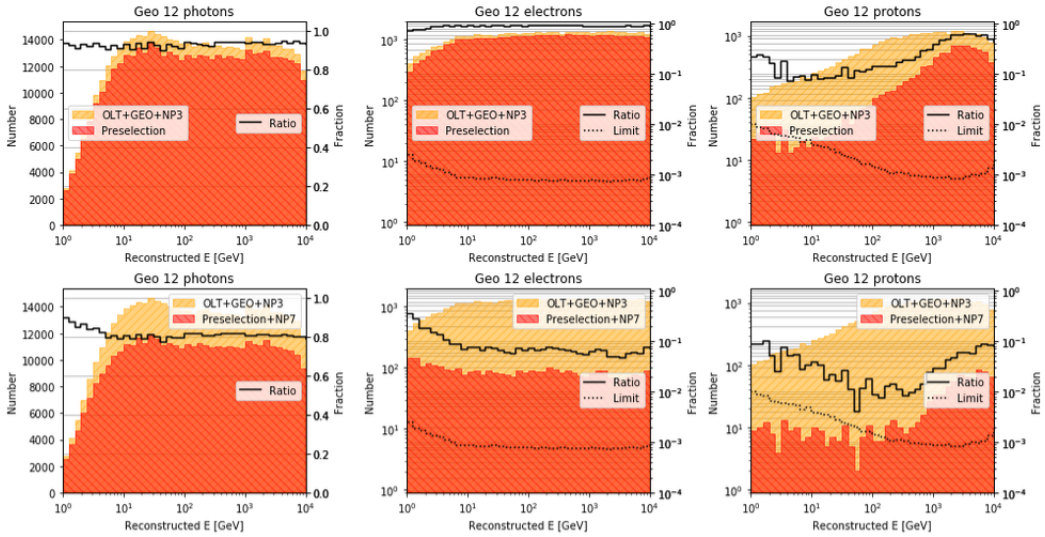

Figure 4: Effect of the quality cuts ("preselection") and the requirement that fewer than 8 layers be used in the tracking ("NP7") for acceptance condition E5. From the left, the columns correspond to photon, electron, and proton primaries. The top row shows the effect of the preselection relative to the combined offline trigger and track reconstruction conditions. The bottom row shows the further effect of the NP7 cut. The yellow and orange histograms correspond to the left axis, whereas the solid and dotted lines correspond to the right axis, showing the result of the cut as a fraction and the limit due to simulated statistics, respectively.

- IMC X8 concentration: fraction of the energy deposited in the layer which is within 1 tungsten Molière radius of track)
- IMC Y8 concentration: as with IMC X8 concentration
- IMC albedo: ratio between energy deposited in the IMC fibers nearest the track in the bottom layer and the topmost layer used in the track reconstruction

Since electron primaries generate identical showers to photons, these cuts will largely reject poorly reconstructed events and proton background. In order to isolate photon events, we must design charge cuts to select charge 0 primaries. We find that a very effective and easily applied charge cut is simply limiting the number of layers used in the tracking. Since all acceptance conditions being studied require passage through the entire IMC, charged particle events predominantly leave energy deposits along the track in every layer of the tracker. Photon events, conversely, generally interact below the first layer of the IMC, and well-reconstructed events will therefore use fewer than eight layers in the tracking. This is illustrated in Figure 4, which shows the impact of this requirement for geometrical condition as an example. While the preselection effectively reduces the number of protons in the dataset, the so-called NP7 cut reduces the electron and proton backgrounds by roughly an order of magnitude.

A charge cut on the CHD is applied to further suppress the charged particle background for the photon analysis. Cuts are derived which maintain 98% of the photon sample for the mean of the hit CHD paddles (shown in Figure 5 and the maximum paddles in each CHD layer. At higher energies (above ~100 GeV), the charge zero measurement in the CHD becomes contaminated by

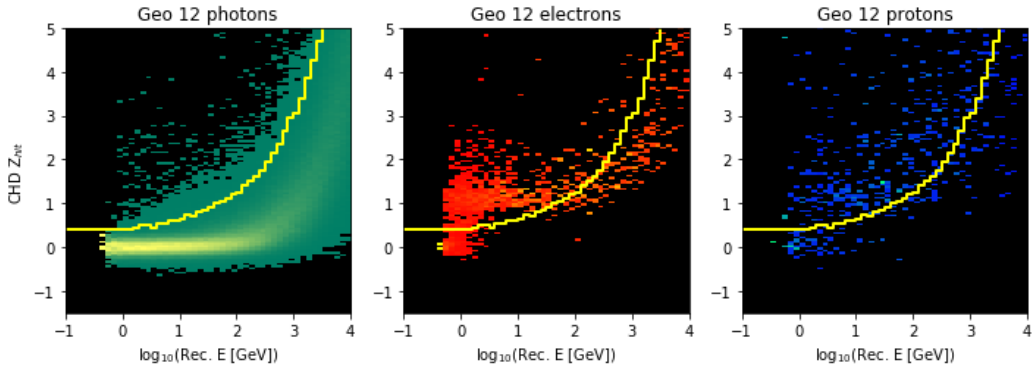

Figure 5: Average of hit CHD paddles for geometry E5 preselected photons, electrons, and protons, respectively, from left to right. The yellow line shows the threshold below which 98% of the photon sample is preserved. The distributions for all three species begin to overlap in the region above a few hundred GeV due to backscattered shower particles.

backscattered shower particles and a cut that preserves the majority of photons also allows many electrons and protons to pass. We turn to the finely segmented IMC to provide a secondary charge cut. Although backscattered particles contaminate this measure of the charge at energies above 1 TeV, cutting at 0.25 MIP for the sum of the hit IMC X1 and IMC Y1 layers is a very effective filter at lower energies. The photon sample is practically unaffected below 100 GeV, and slowly loses efficiency as energy increases above 100 GeV (up to a roughly 10% loss at 1 TeV). With the combination of these four charge cuts, the residual electron and proton contaminations are reduced by more than a factor of 10^3 for all energies beyond the initial selection of events.

4. Results

We have implemented a refinement of the photon event selection, focusing on the efficiency at energies above 10 GeV. The resulting effective area, shown in Figure 6, is relative flat compared to the previous result [2], and has a much larger range of incidence angles allowed. The increases over the existing selection at 200 GeV and 1 TeV are ~35% and ~200%, respectively, for near-normal incidence photons. The increases are larger across the board for events with incidence angles above 15%, and are larger still if geometries E2 and E1 are included. Increases with the inclusion of E0 are limited with the EM track, and it will not be applied for the majority of analyses (except the search for transient counterparts to gamma-ray bursts and gravitational wave events).

5. Conclusion

We are studying the instrument response for the selection described above, including the angular resolution and point-spread function. Further analysis of the backgrounds for the CC Track sample are also being investigated, with the potential for much better sensitivity below 10 GeV (as seen with the previous selection in [2]). Cross validation of these selections as the most effective is being explored with a boosted decision tree approach, and validation of the overall result with comparison to flight data is being finalized. As these efforts conclude, the new selection will be applied to existing gamma-ray analyses with CALET as reported in future conferences.

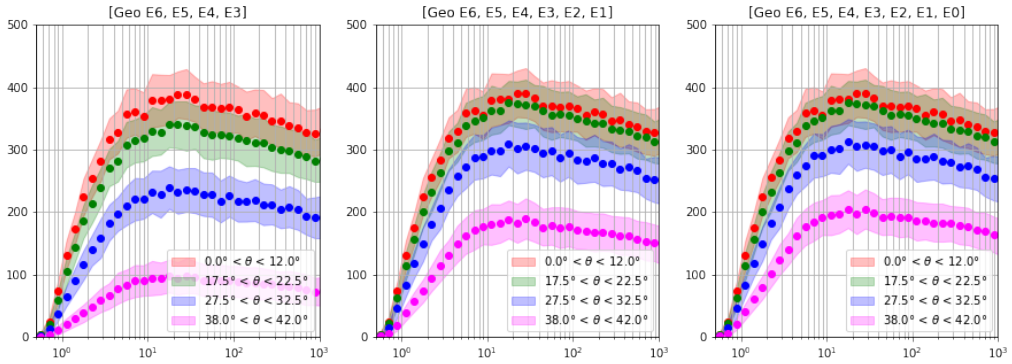

Figure 6: Resulting effective area for the selections described in this work. Units of the x-axis are in GeV, and y-axis are in cm^2. The points are the average for FOV pixels within the four zenith angle ranges indicated in the legend. The shaded region shows the variance of the values for the individual pixels in those bands. The three columns show different combinations of the allowed geometries.

Acknowledgements

We gratefully acknowledge JAXA's contributions to the development of CALET and to the operations onboard the International Space Station. The CALET effort in Italy is supported by ASI under Agreement No. 2013- 018-R.0 and its amendments. The CALET effort in the United States is supported through Grants No. 80NSSC20K0397, No. 80NSSC20K0399, and Np. NNH18ZDA001N-APRA18-004, and under award Np. 80GSFC21M0002. This work was supported in part by JSPS Grant-in-Aid for Scientific Research (S) Grant No. 19H05608 in Japan.

References

[1] S. Torii for the CALET Collaboration, "Highlights from the CALET observations for 7.5 years on the International Space Station," this conference.

[2] N. Cannady et al. (CALET Collaboration), "Characteristics and Performance of the CALorimetric Electron Telescope (CALET) Calorimeter for Gamma-Ray Observations," ApJS 238, 5 (2018).

[3] O. Adriani et al. (CALET Collaboration), "Search for GeV Gamma-Ray Counterparts of Gravitational Wave Events by CALET," ApJ 863:160 (2018).

[4] O. Adriani et al. (CALET Collaboration), "CALET Search for Electronmagnetic Counterparts of Gravitational Waves during the LIGO/Virgo O3 Run," ApJ 933:85 (2022).

[5] Y. Kawakubo for the CALET Collaboration, "CALET Search for electromagnetic counterparts of gravitational waves in O4," this conference.

[6] M. Mori for the CALET Collaboration, "Results from CALorimetric Electron Telescope (CALET) Observations of Gamma-rays on the International Space Station," this conference.

[7] M. Mori for the CALET Collaboration, "High-energy gamma-ray observations above 10 GeV with CALET on the International Space Station," in PoS (ICRC2021) 619, (2019).

[8] Y. Asaoka et al. (CALET Collaboration), "On-Orbit Operations and Offline Data Processing of CALET Onboard the ISS," AP 100, 29–37 (2018).

[9] Y. Asaoka et al. (CALET Collaboration), "Energy Calibration of CALET Onboard the International Space Station," AP 91, 1–10 (2017).

[10] Y. Akaike for the CALET Collaboration, "CALET observational performance expected by CERN beam test," in PoS (ICRC2013) 726 (2013).

Full Author List: CALET Collaboration

O. Adriani[1,2], Y. Akaike[3,4], K. Asano[5], Y. Asaoka[5], E. Berti[2,6], G. Bigongiari[7,8], W.R. Binns[9], M. Bongi[1,2], P. Brogi[7,8], A. Bruno[10], N. Cannady[11,12,13], G. Castellini[6], C. Checchia[7,8], M.L. Cherry[14], G. Collazuol[15,16], G.A. de Nolfo[10], K. Ebisawa[17], A.W. Ficklin[14], H. Fuke[17], S. Gonzi[1,2,6], T.G. Guzik[14], T. Hams[11], K. Hibino[18], M. Ichimura[19], K. Ioka[20], W. Ishizaki[5], M.H. Israel[9], K. Kasahara[21], J. Kataoka[22], R. Kataoka[23], Y. Katayose[24], C. Kato[25], N. Kawanaka[20], Y. Kawakubo[14], K. Kobayashi[3,4], K. Kohri[26], H.S. Krawczynski[9], J.F. Krizmanic[12], P. Maestro[7,8], P.S. Marrocchesi[7,8], A.M. Messineo[8,27], J.W. Mitchell[12], S. Miyake[28], A.A. Moiseev[29,12,13], M. Mori[30], N. Mori[2], H.M. Motz[18], K. Munakata[25], S. Nakahira[17], J. Nishimura[17], S. Okuno[18], J.F. Ormes[31], S. Ozawa[32], L. Pacini[2,6], P. Papini[2], B.F. Rauch[9], S.B. Ricciarini[2,6], K. Sakai[11,12,13], T. Sakamoto[33], M. Sasaki[29,12,13], Y. Shimizu[18], A. Shiomi[34], P. Spillantini[1], F. Stolzi[7,8], S. Sugita[33], A. Sulaj[7,8], M. Takita[5], T. Tamura[18], T. Terasawa[5], S. Torii[3], Y. Tsunesada[35,36], Y. Uchihori[37], E. Vannuccini[2], J.P. Wefel[14], K. Yamaoka[38], S. Yanagita[39], A. Yoshida[33], K. Yoshida[21], and W.V. Zober[9]

[1]Department of Physics, University of Florence, Via Sansone, 1 - 50019, Sesto Fiorentino, Italy, [2]INFN Sezione di Firenze, Via Sansone, 1 - 50019, Sesto Fiorentino, Italy, [3]Waseda Research Institute for Science and Engineering, Waseda University, 17 Kikuicho, Shinjuku, Tokyo 162-0044, Japan, [4]JEM Utilization Center, Human Spaceflight Technology Directorate, Japan Aerospace Exploration Agency, 2-1-1 Sengen, Tsukuba, Ibaraki 305-8505, Japan, [5]Institute for Cosmic Ray Research, The University of Tokyo, 5-1-5 Kashiwa-no-Ha, Kashiwa, Chiba 277-8582, Japan, [6]Institute of Applied Physics (IFAC), National Research Council (CNR), Via Madonna del Piano, 10, 50019, Sesto Fiorentino, Italy, [7]Department of Physical Sciences, Earth and Environment, University of Siena, via Roma 56, 53100 Siena, Italy, [8]INFN Sezione di Pisa, Polo Fibonacci, Largo B. Pontecorvo, 3 - 56127 Pisa, Italy, [9]Department of Physics and McDonnell Center for the Space Sciences, Washington University, One Brookings Drive, St. Louis, Missouri 63130-4899, USA, [10]Heliospheric Physics Laboratory, NASA/GSFC, Greenbelt, Maryland 20771, USA, [11]Center for Space Sciences and Technology, University of Maryland, Baltimore County, 1000 Hilltop Circle, Baltimore, Maryland 21250, USA, [12]Astroparticle Physics Laboratory, NASA/GSFC, Greenbelt, Maryland 20771, USA, [13]Center for Research and Exploration in Space Sciences and Technology, NASA/GSFC, Greenbelt, Maryland 20771, USA, [14]Department of Physics and Astronomy, Louisiana State University, 202 Nicholson Hall, Baton Rouge, Louisiana 70803, USA, [15]Department of Physics and Astronomy, University of Padova, Via Marzolo, 8, 35131 Padova, Italy, [16]INFN Sezione di Padova, Via Marzolo, 8, 35131 Padova, Italy, [17]Institute of Space and Astronautical Science, Japan Aerospace Exploration Agency, 3-1-1 Yoshinodai, Chuo, Sagamihara, Kanagawa 252-5210, Japan, [18]Kanagawa University, 3-27-1 Rokkakubashi, Kanagawa, Yokohama, Kanagawa 221-8686, Japan, [19]Faculty of Science and Technology, Graduate School of Science and Technology, Hirosaki University, 3, Bunkyo, Hirosaki, Aomori 036-8561, Japan, [20]Yukawa Institute for Theoretical Physics, Kyoto University, Kitashirakawa Oiwake-cho, Sakyo-ku, Kyoto, 606-8502, Japan, [21]Department of Electronic Information Systems, Shibaura Institute of Technology, 307 Fukasaku, Minuma, Saitama 337-8570, Japan, [22]School of Advanced Science and Engineering, Waseda University, 3-4-1 Okubo, Shinjuku, Tokyo 169-8555, Japan, [23]National Institute of Polar Research, 10-3, Midori-cho, Tachikawa, Tokyo 190-8518, Japan, [24]Faculty of Engineering, Division of Intelligent Systems Engineering, Yokohama National University, 79-5 Tokiwadai, Hodogaya, Yokohama 240-8501, Japan, [25]Faculty of Science, Shinshu University, 3-1-1 Asahi, Matsumoto, Nagano 390-8621, Japan, [26]Institute of Particle and Nuclear Studies, High Energy Accelerator Research Organization, 1-1 Oho, Tsukuba, Ibaraki, 305-0801, Japan, [27]University of Pisa, Polo Fibonacci, Largo B. Pontecorvo, 3 - 56127 Pisa, Italy, [28]Department of Electrical and Electronic Systems Engineering, National Institute of Technology (KOSEN), Ibaraki College, 866 Nakane, Hitachinaka, Ibaraki 312-8508, Japan, [29]Department of Astronomy, University of Maryland, College Park, Maryland 20742, USA, [30]Department of Physical Sciences, College of Science and Engineering, Ritsumeikan University, Shiga 525-8577, Japan, [31]Department of Physics and Astronomy, University of Denver, Physics Building, Room 211, 2112 East Wesley Avenue, Denver, Colorado 80208-6900, USA, [32]Quantum ICT Advanced Development Center, National Institute of Information and Communications Technology, 4-2-1 Nukui-Kitamachi, Koganei, Tokyo 184-8795, Japan, [33]College of Science and Engineering, Department of Physics and Mathematics, Aoyama Gakuin University, 5-10-1 Fuchinobe, Chuo, Sagamihara, Kanagawa 252-5258, Japan, [34]College of Industrial Technology, Nihon University, 1-2-1 Izumi, Narashino, Chiba 275-8575, Japan, [35]Graduate School of Science, Osaka Metropolitan University, Sugimoto, Sumiyoshi, Osaka 558-8585, Japan, [36]Nambu Yoichiro Institute for Theoretical and Experimental Physics, Osaka Metropolitan University, Sugimoto, Sumiyoshi, Osaka 558-8585, Japan, [37]National Institutes for Quantum and Radiation Science and Technology, 4-9-1 Anagawa, Inage, Chiba 263-8555, Japan, [38]Nagoya University, Furo, Chikusa, Nagoya 464-8601, Japan, [39]College of Science, Ibaraki University, 2-1-1 Bunkyo, Mito, Ibaraki 310-8512, Japan

PoS(ICRC2023)657